

Ampere-Level 4000 h Parallel Alcohols Electro-Refinery and Hydrogen Production

Pengju Yang, Kaizhou Yang, Jieshan Qiu, and Zhiyu Wang*

Coupling electro-refinery with water electrolysis paves a sustainable pathway for parallel production of value-added chemicals and hydrogen. However, its practical feasibility remains hindered by large overpotentials, unsatisfactory selectivity, and inadequate durability. Here, we report a pH-asymmetric hybrid system of electrolysis (AHSE) to realize ampere-level, long-term alcohols electro-refinery and parallel hydrogen production. By harnessing internal neutralization energy, the AHSE simultaneously produces benzoic acid (Ph-COOH) and hydrogen at a low electricity expense of 3.19–3.78 kWh per m^3 H_2 at 500 mA cm^{-2} , saving 24.6–30.6% energy than pH-symmetric systems. The operational stability is maximized by independent optimization of pH conditions at the anode and cathode, allowing for continuous operation over 4100 h at large current densities of 500–1000 mA cm^{-2} . High Faradaic efficiency (FE) of 91.3–97.7% is reached for benzyl alcohol (BA) conversion, with 78.5–95.5% Ph-COOH selectivity. When scaled up 100 folds, the AHSE retains over 85% FE for BA conversion and 88.5% Ph-COOH selectivity while yielding hydrogen at a fast rate of 18.7 L h^{-1} at an ultra-high current of 50 A at 3.14 V.

1. Introduction

Water electrolysis represents the most efficient pathway for green hydrogen production as a sustainable alternative to fossil fuels.^[1] However, this technology demands substantial freshwater resources, which are both limited and unevenly distributed worldwide. Seawater electrolysis emerges as a viable solution for

cost-effective, grid-scale hydrogen production while mitigating water scarcity, particularly when integrated with offshore wind or solar farms.^[2] Despite its promise, practical deployment of seawater electrolysis still faces several critical challenges: i) anode degradation induced by corrosive species (e.g., Cl_2 , ClO^-) released from the competitive electrochemical oxidation of abundant Cl^- (ClOR) during oxygen evolution reaction (OER); ii) cathode passivation due to Ca(OH)_2 and Mg(OH)_2 precipitation, driven by local pH increases during hydrogen evolution reaction (HER); iii) high potential barrier of OER and ClOR, leading to unaffordable electricity expense at large currents.^[3–5] To overcome these limitations, recent efforts have focused on developing corrosion-resistant, high-performance electrocatalysts to enhance the durability and efficiency of seawater electrolysis.^[6–8] Notably, direct seawater electrolysis has been achieved by utilizing a self-breathable waterproof membrane

to mitigate chlorine corrosion in the seawater electrolyzer.^[2] Nevertheless, existing seawater electrolyzers still consume electricity greater than 4–6 kWh per m^3 H_2 , limiting their large-scale deployment.^[6,8,9]

The electrocatalytic refinery offers a sustainable route for on-demand, decentralized production of high-value chemicals with superior energy efficiency and fewer emissions.^[10–14] Replacing energy-intensive OER and ClOR with thermodynamically more favorable electrocatalytic refining processes holds great potential for reducing overall energy consumption in hydrogen production. The resulting hybrid water electrolysis systems not only avoid chloride-induced anode corrosion but also generate value-added chemicals to offset hydrogen costs.^[15] The electrocatalytic conversion of various organics, including alcohols, aldehydes, amides, and alkenes, has been explored to enhance the energy efficiency and cost-effectiveness of hydrogen production.^[16–21] However, its practical feasibility remains hindered by high overpotentials, unsatisfactory selectivity, and limited durability, arising from complex reaction pathways involving multi-proton-coupled electron transfers and uncontrolled side reactions. For instance, alcohol oxidation reactions (AOR) theoretically enable substantial energy savings due to their low thermodynamic potentials (<0.3 V).^[22–26] However, this benefit is diminished by high overpotentials (>0.7–0.8 V) and sluggish kinetics associated with multi-step dehydrogenation and carbonylation

P. Yang, K. Yang, Z. Wang
State Key Lab of Fine Chemicals, Frontiers Science Center for Smart
Materials Oriented Chemical Engineering
Liaoning Key Lab for Energy Materials and Chemical Engineering
School of Chemical Engineering
Dalian University of Technology
Dalian 116024, China
E-mail: zywang@dlut.edu.cn

Z. Wang
School of Chemical Engineering and Technology
Xinjiang University
Urumqi 830046, China

J. Qiu
College of Chemical Engineering
Beijing University of Chemical Technology
Beijing 100029, China

The ORCID identification number(s) for the author(s) of this article can be found under <https://doi.org/10.1002/adfm.202510160>

DOI: 10.1002/adfm.202510160

reactions involving multiple charge transfers. Consequently, electrolysis lifespan remains limited to less than 400–500 h at current densities below 500 mA cm⁻², falling short of meeting industrial demands.^[27–30]

The Nernst equation ($\Delta G = -zFE_{MF}$) suggests that internal chemical energy can be harnessed to reduce the energy demands of water electrolysis.^[31,32] For example, the neutralization energy of the acid-base reaction ($H^+ + OH^- \rightarrow H_2O$) releases a reaction heat (ΔH^θ) of -55.83 kJ mol⁻¹ at 298.15 K. Notably, this spontaneous reaction also exhibits a positive entropic heat ($T\Delta S^\theta = 24.05$ kJ mol⁻¹, 298.15 K), allowing heat extraction from not only the reaction itself but also the surrounding environment to drive electrical work.^[33,34] A sum of these energy contributes to a total Gibbs free energy change of -79.88 kJ mol⁻¹ at 298.15 K, potentially reducing the electrolysis voltage by 0.828 V under a pH gradient of 14 between the anode and cathode.^[31,33] Meanwhile, acidic and alkaline waste constitutes major industrial sewage, with global discharge exceeding billion tons annually. Their neutralization theoretically releases over 1200 TWh of energy, translating to 17–21 megatons of hydrogen beyond the *International Energy Agency's* (IEA) 2030 target for low-carbon hydrogen production (17 megatons).^[32] Thus, utilization of the acid-base neutralization energy presents a promising strategy for cost-effective hydron production while addressing the environmental hazards of corrosive and toxic pollutants.

Herein, we report an asymmetric hybrid system of electrolysis (AHSE) for harnessing neutralization energy to overcome the high overpotential obstacle in an electrocatalytic refinery. The AHSE is designed by coupling acidic HER in seawater with electro-oxidation of organics under alkaline conditions. As a demonstration of the efficacy of the system in electro-refinery, the AOR is employed due to its potential for producing value-added derivatives such as aldehydes and carboxylic acids.^[35,36] By integrating a Co-doped Ni₂P electrode as the anode in AHSE, efficient hydrogen production is achieved alongside benzyl alcohol (BA) conversion to benzoic acid (Ph-COOH) with high selectivity at a low voltage of ca. 1.45–2.2 V (without *iR* correction) under industrial-level current densities of 500–1000 mA cm⁻² for 4,100 h. The 100 fold scaled AHSE reaches a high FE of 90% for hydrogen production and over 88% selectivity for Ph-COOH generation at an ultra-high current of 50 A.

2. Results and Discussion

2.1. Fabrication of Co-Ni₂P/NF Electrode

A Co-doped Ni₂P electrode (Co-Ni₂P/NF) is made by phosphatization of Co-doped Ni(OH)₂ nanosheet arrays on nickel foam (NF) to lower the intrinsic overpotential of BA oxidation reaction (BOR) in alkaline medium (Figure 1a,b; Figure S1a, Supporting Information). EDS mapping confirms the existence of Co, Ni, and P elements in Co-Ni₂P with a Co doping amount of 9.9 wt.% (Figure 1c). Doping of Co with a larger atomic radius induces a slight shift of diffraction peak from the (111), (201), and (210) plane of Ni₂P toward lower angles in XRD patterns, leading to a lattice expansion of ca. 0.18%, 0.2% and 0.21% along these directions, respectively (Figure 1d). This accompanies charge redistribution via electron transfer from Co to neighboring Ni, as evi-

denced by X-ray photoelectron spectroscopy (XPS) spectra, where the peaks from the Ni–P bond negatively shift by 0.35 eV, while the peaks of the Co–P bond move to the opposite direction by 0.39 eV relative to undoped samples (Figure 1e–f). Additionally, the O 1s XPS spectra reveal that surface oxide species on Co-Ni₂P are mainly P–O and metal–OH, whereas undoped Ni₂P exhibits merely P–O species (Figure S2, Supporting Information). X-ray absorption near-edge structure (XANES) spectra verify that both Ni and Co in Co-Ni₂P adopt valence states ranging from 0 to +2 (Figure 1g,h). Compared to the undoped sample, the Ni absorption edge of Co-Ni₂P shifts to lower energy while the Co absorption edge moves to higher energy, indicating charge transfer from Co dopant to Ni. Fourier-transform extended XAFS (FT-EXAFS) spectra and fitting data further reveal that charge redistribution and localized lattice tensile induced by Co doping extend the Ni–P bond length from 2.19 Å in Ni₂P to 2.22 Å upon Co doping (Figure 1i,j; Figures S3 and S4, Tables S1 and S2, Supporting Information). These effects upshift the *d*-band center of Ni and weaken Ni–P bonds (Figure S1b, Supporting Information), thereby facilitating surface hydroxylation of Co-Ni₂P to form active intermediates such as NiOOH upon electrochemical oxidation, which in turn promotes BOR.^[37] The absence of Co–Co bonds suggests atomic dispersion of Co within the Ni₂P lattice via Co–P and Co–Ni coordination.

2.2. BOR Performance of Co-Ni₂P/NF Electrode

The intrinsic BOR activity of the Co-Ni₂P/NF electrode is assessed in 1.0 M KOH containing 0.1 M BA, with all potentials referenced to the reversible hydrogen electrode (RHE) unless otherwise specified. For comparison, benchmark electrodes, including Ni₂P/NF and Co₂P/NF, are prepared by loading Ni₂P or Co₂P onto NF, respectively. The active mass loading is ca. 1.7 mg cm⁻² for all electrodes. The undoped Ni₂P/NF exhibits a greatly lower potential (1.39 V) than Co₂P/NF (1.53 V) at a current density of 500 mA cm⁻², indicating the limited activity of Co₂P for BOR. However, its BOR activity remains unsatisfactory, particularly at high current densities, due to the sluggish formation of active γ -NiOOH intermediate and limited reactant adsorption. Co-doping (Ni: Co = 9: 1) further reduces the potential for BOR to 1.35 V at 500 mA cm⁻² (Figure 2a). This performance surpasses that of reported BOR electrocatalysts, which typically operate at lower current densities (e.g., 100 mA cm⁻²) while requiring higher potentials (1.36–1.55 V) (Figure 2b; Table S3, Supporting Information). Excess Co doping (e.g., Ni: Co = 4: 1) reduces the concentration of Ni sites and suppresses γ -NiOOH generation, thereby compromising BOR activity at large current densities. The Co-Ni₂P/NF electrode exhibits high selectivity toward BOR even at high current density, reflected by its significantly higher potential of 1.67 V for OER at 500 mA cm⁻² in 1.0 M KOH (Figure 2c). This electrode exhibits high stability toward BOR for 120 h at 500 mA cm⁻², maintaining much lower potentials than OER (Figure 2d). After BOR, inductively coupled plasma optical emission spectroscopy (ICP-OES) analysis reveals minimal leaching of Ni and Co from the Co-Ni₂P detached from the NF (Table S4, Supporting Information), demonstrating its high structural and chemical stability. The gradual potential rise from 1.6 to 1.75 V (without *iR* correction) every 40 h is due to BA depletion in the

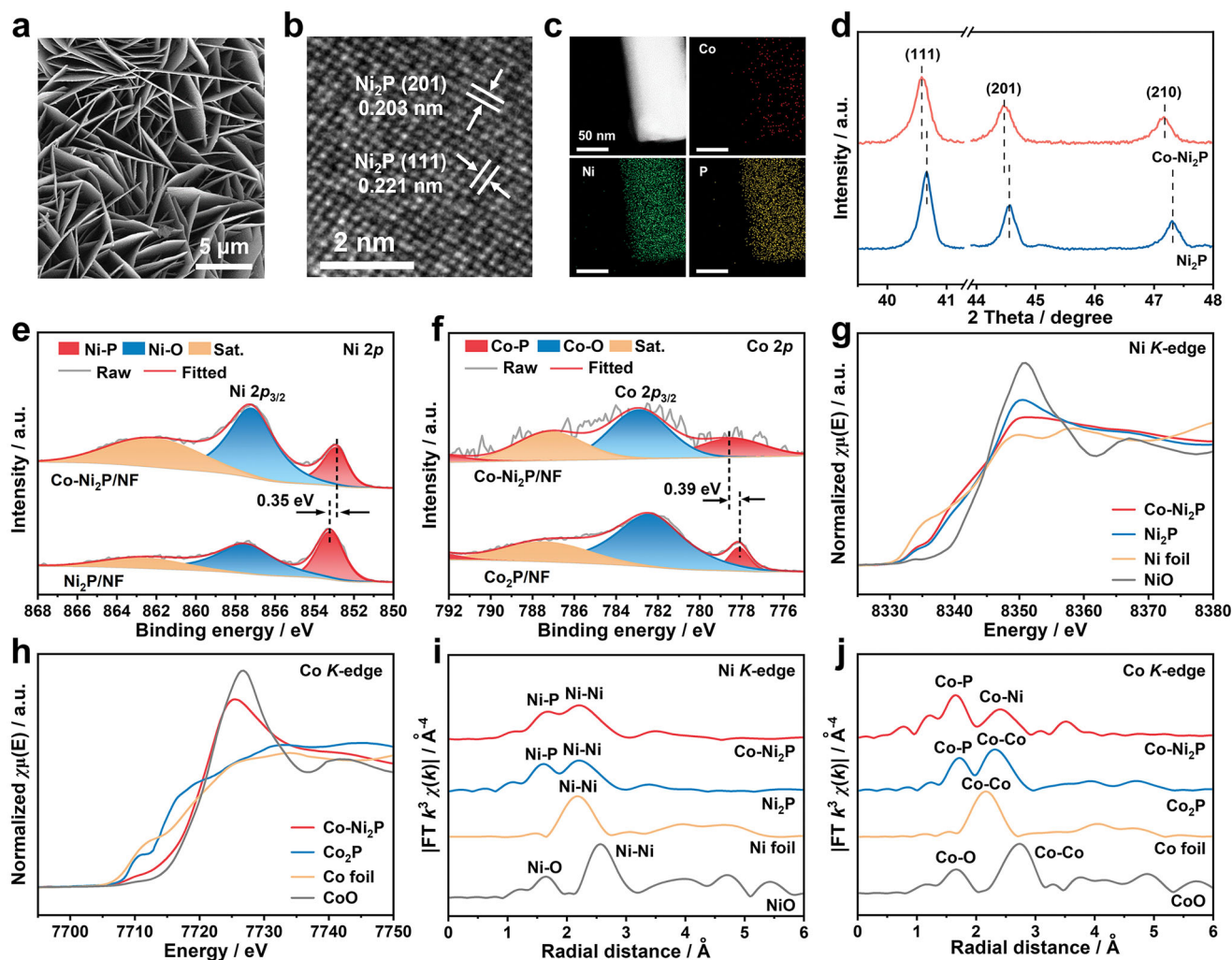


Figure 1. Characterization of Co-Ni₂P/NF electrode. a) SEM and b) HRTEM images of Co-Ni₂P nanosheets on NF substrate. c) Elemental mapping showing the existence of Co, Ni, and P elements in Co-Ni₂P. d) XRD patterns of Co-Ni₂P and Ni₂P detached from NF. e) Ni 2p XPS spectra of Co-Ni₂P/NF and Ni₂P/NF. f) Co 2p XPS spectra of Co-Ni₂P/NF and Co₂P/NF. g) Ni K-edge and (h) Co K-edge XANES spectra of Co-Ni₂P and benchmark samples. i, j) The corresponding k^3 -weighted FT-EXAFS spectra of Co-Ni₂P and benchmark samples.

electrolyte, which can be reversed by replenishing the BA-containing electrolyte.

High-performance liquid chromatography (HPLC) identifies Ph-COOH as the primary product of BOR over the Co-Ni₂P/NF electrode, with only a trace amount of by-products such as benzaldehyde (Ph-CHO) (Figure S5, Supporting Information). This electrode achieves a maximum FE of 98.3% for BOR and Ph-COOH selectivity of 97.4% at 1.6 V, with a rapid BA conversion rate of 4.11 mmol cm⁻² h⁻¹ (Figure 2e). In a potential range of 1.4–1.8 V, it maintains a high FE of 95.7–98.3% for BOR and Ph-COOH selectivity of 95.4–97.4% (Figure 2f–g). In contrast, undoped Ni₂P/NF exhibits lower FE (91.4–96.2%) and Ph-COOH selectivity (59.9–81.7%) over the same potential range, with a slower BA conversion rate of 3.5 mmol cm⁻² h⁻¹ at 1.6 V. HPLC analysis at various charge inputs (200 C, 400 C, and 1000 C) between 1.4–1.8 V reveal largely suppressed formation of the Ph-CHO by-products on Co-Ni₂P/NF compared to Ni₂P/NF, accounting for significant selectivity gap between the two catalysts

(Figure S6, Supporting Information). Chronoamperometry test at 1.6 V until full theoretical charge transfer yields a BA conversion efficiency of 98.7%, a Ph-COOH yield of 98.2%, and an overall FE exceeding 97.9% (Figure 2h). Even at 1.9 V, the Co-Ni₂P/NF retains a high FE of 95.5% for BOR, whereas extensive OER on Ni₂P/NF reduces its FE to 87.7%, highlighting the crucial role of Co doping in enhancing BOR selectivity of Co-Ni₂P.

2.3. Mechanism of BOR Improvement on Co-Ni₂P/NF Electrode

After BOR, the Co-Ni₂P/NF retains its original architecture but undergoes notable surface morphological changes (Figure S7a–c, Supporting Information). The marked reduction of metal-P and P–O bonds, accompanied by a substantial increase in Ni–OH species, further indicates the surface reconstruction of Co-Ni₂P into Co-doped Ni(OH)_x during alkaline BOR (Figure S7d–g, Supporting Information).^[28] To identify the active phase, in situ

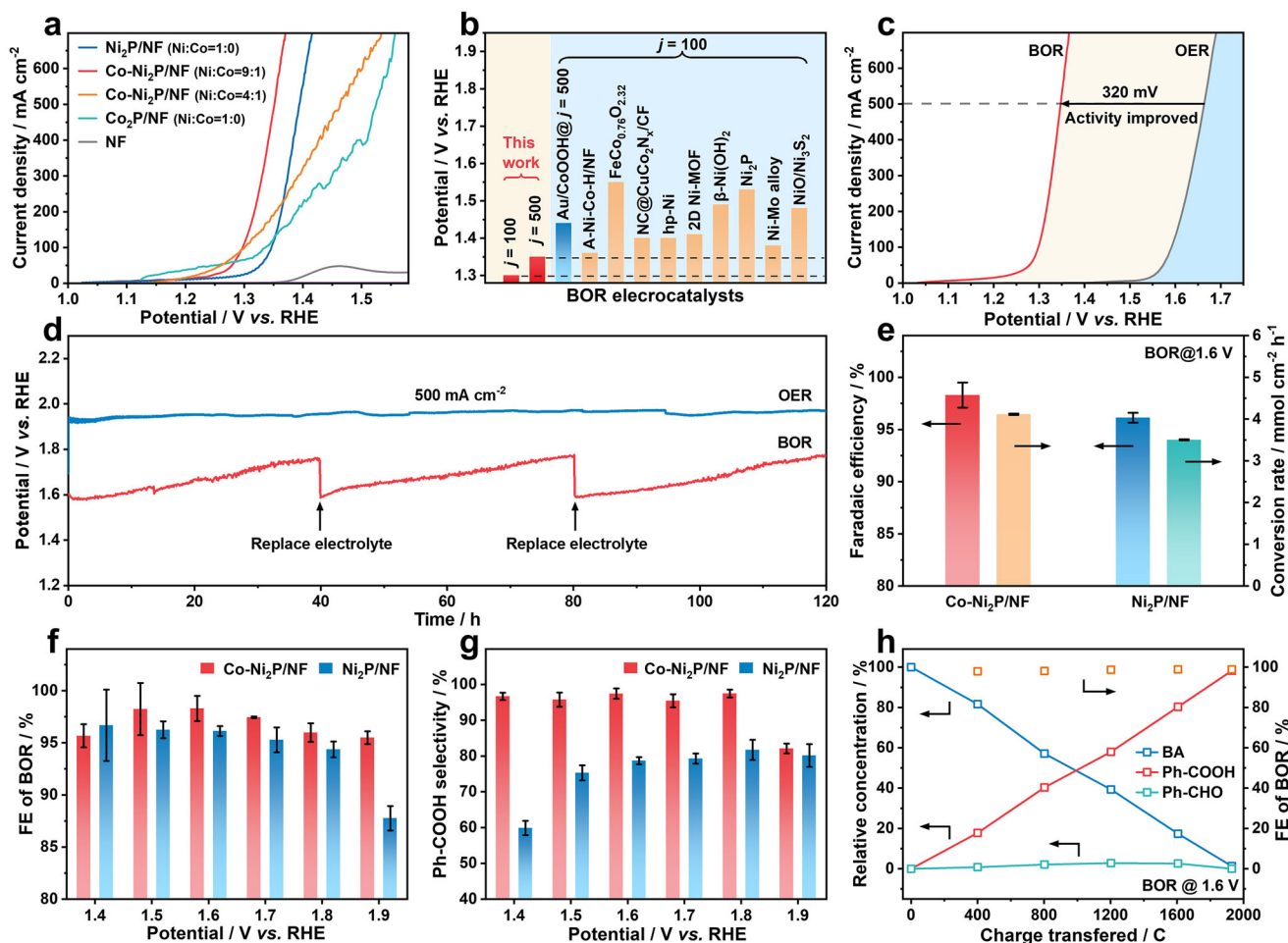


Figure 2. Electrocatalytic performance of Co-Ni₂P/NF for BOR. a) LSVs of Co-Ni₂P/NF with different Co doping amounts, Ni₂P/NF, Co₂P/NF, and NF for BOR. b) A comparison between Co-Ni₂P/NF and reported electrocatalysts in BOR activity. c) A comparison between BOR and OER over Co-Ni₂P/NF in 1.0 M KOH in anode potential. d) The durability of Co-Ni₂P/NF for BOR and OER at a current density of 500 mA cm⁻². e) A comparison between Co-Ni₂P/NF and Ni₂P/NF in FE and BA conversion rate for BOR at 1.6 V. A comparison between Co-Ni₂P/NF and Ni₂P/NF in (f) FE and (g) Ph-COOH selectivity for BOR at different potentials. h) The variation of the relative concentration of BA, Ph-COOH, and Ph-CHO during BOR on Co-Ni₂P/NF at 1.6 V.

Raman spectroscopy analyses are performed on Co-Ni₂P/NF during BOR. As the applied potential exceeds 1.4 V, two bands appear at 457 and 535 cm⁻¹, which gradually shift to 465 and 544 cm⁻¹ with increasing intensity until 1.7 V, respectively (Figure 3a). The Raman shift and relative intensity ratio of these two peaks closely align with the ϵ_g bending vibration ($\delta(\text{Ni}^{\text{III}}\text{-O})$) and A_{1g} stretching vibration ($\nu(\text{Ni}^{\text{III}}\text{-O})$) of γ -NiOOH.^[38,39] Due to the chemical interaction between BA and γ -NiOOH, these vibrational bands undergo a redshift compared to the OER case (Figure S8a, Supporting Information).^[40,41] Upon returning to open-circuit potential (OCP), the bands of γ -NiOOH disappear, confirming that γ -NiOOH acts as the active phase for catalyzing alkaline BOR. No Raman signals from γ -NiOOH are detected on Ni₂P/NF during BOR up to 1.7 V in 1.0 M KOH containing 0.1 M BA (Figure 3a). However, the γ -NiOOH bands appear when BA concentration falls below 0.06 M at a fixed potential of 1.6 V (Figure S8b, Supporting Information). This observation indicates rapid consumption of γ -NiOOH once formed on Ni₂P/NF, thereby limiting its BOR activity and selectivity at large current densities.

In situ Fourier-transform infrared reflection (FT-IR) spectra further validate γ -NiOOH formation on Co-Ni₂P above 1.4 V, evidenced by the rise of hydroxyl stretching vibration bands at 3600–3720 cm⁻¹, whereas Ni₂P surface maintains unchanged (Figure 3b).^[42] These findings suggest that γ -NiOOH acts as the active phase for catalyzing alkaline BOR on both Co-Ni₂P and undoped Ni₂P. However, Co doping promotes γ -NiOOH generation at lower potentials and a faster rate that outpaces its consumption, thereby enhancing BOR performance, particularly selectivity. This effect arises from the lower oxidation state of Ni and elongated Ni–P bond length induced by Co doping, which enhances the activity of Ni sites toward surface hydroxylation during alkaline BOR.

To validate the enhanced γ -NiOOH formation on Co-Ni₂P, cyclic voltammetry (CV) tests are conducted in the absence of BA to eliminate its reductive effect on γ -NiOOH. Significantly reduced potential barrier and improved kinetics of γ -NiOOH formation on Co-Ni₂P/NF are reflected by a stronger redox peak, with more than twice higher oxidation charge density at a lower

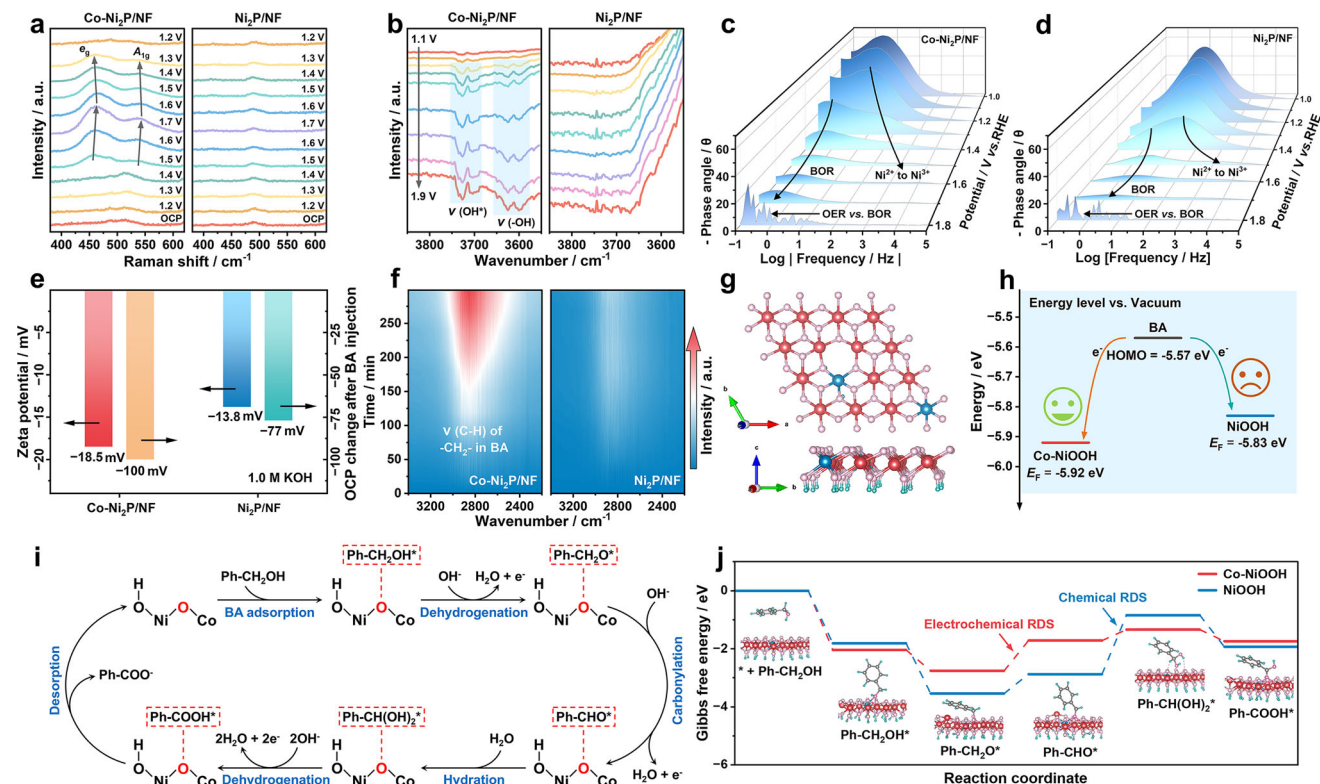


Figure 3. BOR mechanism of Co-Ni₂P/NF. a) In situ Raman spectra and b) in situ FT-IR spectra showcasing the evolution of intermediate species on Co-Ni₂P/NF and Ni₂P/NF during BOR at varying potentials. In-situ EIS spectra of (c) Co-Ni₂P/NF and (d) Ni₂P/NF during BOR at varying potentials. e) A comparison between Co-Ni₂P/NF and Ni₂P/NF in Zeta potential in 1.0 M KOH and the OCP change after BA injection. f) FT-IR spectra reveal the variation of BA adsorption on Co-Ni₂P/NF and Ni₂P/NF. g) Structural model of the Co-NiOOH (001) surface for DFT calculations, the spheres in red, blue, pink, and turquoise represent Ni, Co, O, and H atoms, respectively. (h) The HOMO level of BA and the E_F of Co-NiOOH and NiOOH. i) Schematic illustration of the BOR pathway on Co-NiOOH. j) Gibbs free energy diagrams for BOR pathways on Co-NiOOH and NiOOH.

potential (1.35 V) and a smaller Tafel slope (34.2 mV dec⁻¹) compared to Ni₂P/NF (1.41 V, 41.0 mV dec⁻¹) (Figure S9, Supporting Information). The beneficial role of Co doping in promoting γ -NiOOH formation and enhancing BOR activity is further validated by *in-situ* electrochemical impedance spectroscopy (EIS). In the Bode plots, the low-frequency region (0.1–10 Hz) corresponds to interfacial charge transfer during BOR, while the high-frequency region (10–1000 Hz) is associated with charge transfer associated with Ni(OH)_x electro-oxidation to γ -NiOOH (Figure 3c,d).^[28,43] As the potential rises from 1.2 to 1.5 V, the Co-Ni₂P/NF exhibits a significantly faster decline of phase angle in both frequency regions relative to Ni₂P/NF, indicating superior kinetics for both γ -NiOOH formation and BOR.

Since γ -NiOOH formation initiates via OH⁻ attack to Ni(OH)_x (Ni(OH)_x + OH⁻ → γ -NiOOH + H₂O + e⁻), the OH⁻ adsorption capability of the electrodes is crucial for accelerating γ -NiOOH generation. On both Co-Ni₂P/NF and Ni₂P/NF, the CVs exhibit a broad peak at ca. 0.85 V corresponding to OH⁻ adsorption in 1.0 M KOH (Figure S10, Supporting Information).^[43] Compared to Ni₂P (ζ = -13.8 mV), the Co-Ni₂P/NF displays a higher CV peak current and a more negative Zeta potential (ζ = -18.5 mV) (Figure 3e). It indicates enhanced OH⁻ adsorption in the inner Helmholtz layer, thereby promoting Ni(OH)_x electro-oxidation to γ -NiOOH.^[44] On this basis, the OCP variation of the electrodes is monitored to track interfacial charge re-

distribution induced by BA adsorption.^[44] Following BA injection into 1.0 M KOH, the Co-Ni₂P/NF exhibits a larger OCP drop (100 mV) than Ni₂P/NF (77 mV), reflecting stronger BA adsorption (Figure 3e; Figure S11, Supporting Information). The FT-IR spectroscopy at OCP further supports this, showing a rapid increase in the intensity of C-H stretching vibration bands (ν (C-H)) at 2700–3000 cm⁻¹ from the -CH₂- group in BA on Co-Ni₂P/NF over time, whereas Ni₂P/NF displays weak signals (Figure 3f).^[42] Electrochemical adsorbate-stripping measurements also exhibit a higher oxidation charge density for BA adsorption on Co-Ni₂P/NF than on Ni₂P/NF (0.41 vs 0.28 C cm⁻²) (Figure S12, Supporting Information).^[17] These observations suggest that Co doping facilitates not only γ -NiOOH formation but also reactant adsorption, thereby improving BOR activity.

Density functional theory (DFT) calculations are performed on the typical (001) surface of Co-doped NiOOH (Co-NiOOH) and undoped NiOOH to understand the BOR mechanism (Figure 3g; Figure S13, Supporting Information). The Co-NiOOH exhibits a lower Fermi level (E_F = -5.92 eV) than NiOOH (-5.83 eV), generating a greater electrochemical potential difference (μ) between its E_F and the highest occupied molecular orbital (HOMO) energy level of BA (-5.57 eV). This improvement facilitates the construction of electron transfer channels between BA and Co-NiOOH, thereby promoting BOR kinetics (Figure 3h).^[45] This is consistent with the smaller charge transfer impedance

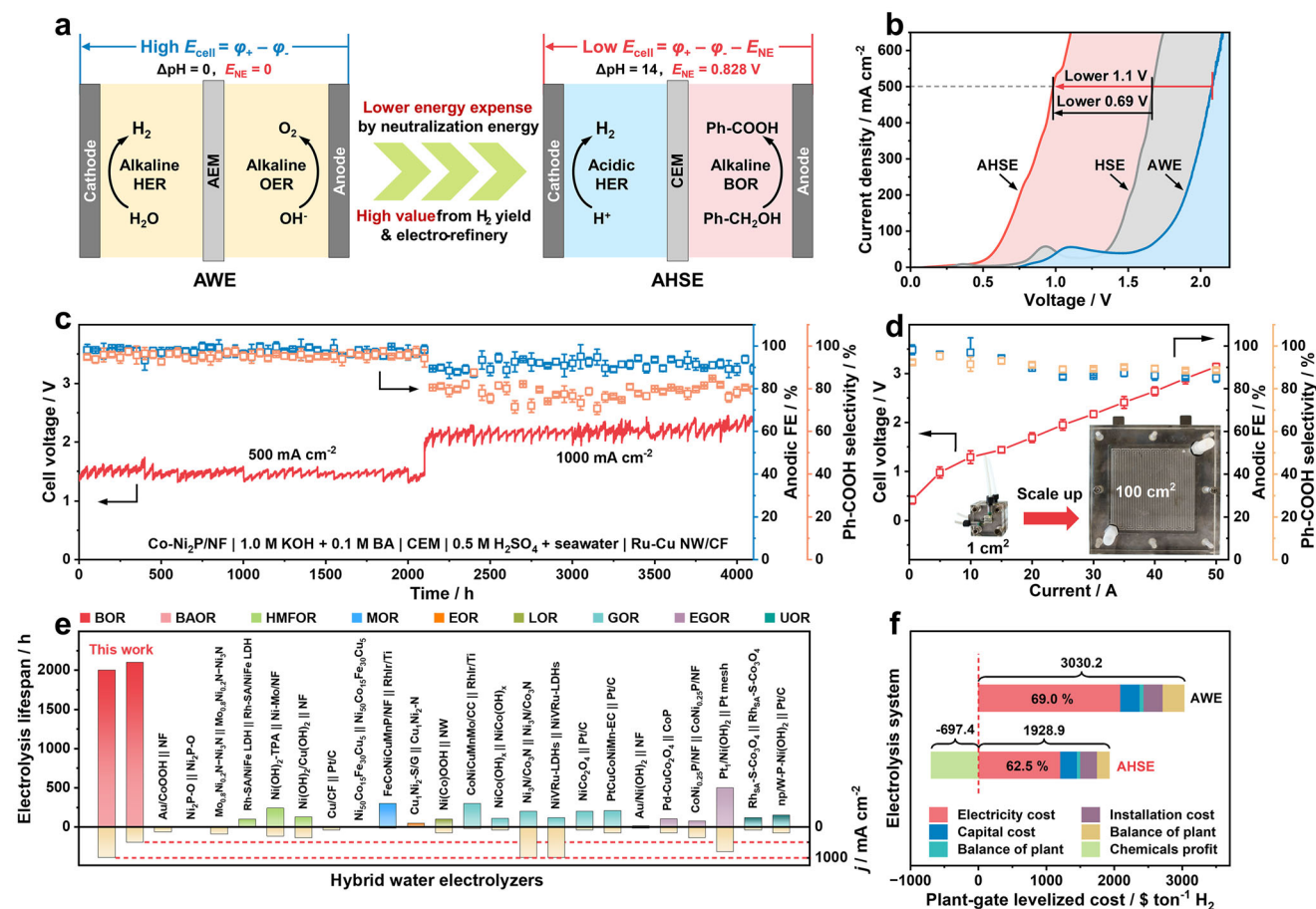


Figure 4. AHSE Performance for ampere-level hydrogen and Ph-COOH production. a) Schematic illustration of the benefits of AHSE over AWE. b) LSVs of AHSE coupling acidic HER and alkaline BOR, HSE coupling alkaline HER and BOR, and AWE coupling alkaline HER and OER. c) The long-term durability of AHSE for 4100 h at 500 and 1000 mA cm⁻². d) Cell voltages, anodic Faradic efficiency, and Ph-COOH selectivity of AHSE scaled up to 100 cm² at various currents. e) A comparison of AHSE with reported hybrid water electrolyzers coupling organics electro-refinery in electrolysis lifespan and current densities. f) A rough techno-economic analysis of AHSE using BA wastewater as the anolyte feedstock, compared to renewables-powered AWE.

(R_{ct} , 1.44 Ω) and Tafel slope (61 mV dec⁻¹) of Co-Ni₂P compared to Ni₂P (4.88 Ω , 69 mV dec⁻¹) for alkaline BOR (Figure S14, Supporting Information). On both Co-NiOOH and NiOOH, the BOR proceeds via initial BA adsorption, followed by sequential dehydrogenation to Ph-CH₂O*, carbonylation to Ph-CHO*, hydration to Ph-CH(OH)₂*, and eventually dehydrogenation to form Ph-COOH* (Figure 3j). No stable Ph-C(OH)₂* intermediate is identified as its rapid conversion to carboxylic acids occurs via electrophilic attack of OH* in alkaline media.^[46] Gibbs free energy diagram shows that the BA adsorption and its dehydrogenation (Ph-CH₂OH* + OH⁻ → Ph-CH₂O* + H₂O + e⁻) are exothermic on both Co-NiOOH and NiOOH (Figure 3j). On Co-NiOOH, the subsequent carbonylation step (Ph-CH₂O* + OH⁻ → Ph-CHO* + H₂O + e⁻, $\Delta G = 1.04 \text{ eV}$) presents the primary energy barrier, followed by a relatively moderate uphill hydration step (Ph-CHO* + H₂O → Ph-CH(OH)₂*, $\Delta G = 0.38 \text{ eV}$). Thus, the carbonylation of Ph-CH₂O* to Ph-CHO* is identified as the rate-determining step (RDS) in BOR on Co-NiOOH. Whereas on NiOOH, both the carbonylation of Ph-CH₂O* to Ph-CHO* and the subsequent hydration to Ph-CH(OH)₂* remain thermodynamically unfavorable, with the latter step being more endothermic ($\Delta G = 2.03 \text{ eV}$).

This high energy barrier impedes the overall reaction and promotes the undesired formation of Ph-CHO to reduce Ph-COOH selectivity. Shifting the RDS from a slow surface chemical transformation to a more efficient electrochemical step substantially enables faster reaction kinetics and precise control over the reaction pathway. This mechanistic advantage accounts for the significantly enhanced BOR performance of Co-Ni₂P, particularly its Ph-COOH selectivity at large current densities.

2.4. AHSE Performance for Ampere-Level Hydrogen and Ph-COOH Production

An AHSE is engineered by integrating acidic HER in seawater at the cathode with alkaline BOR at the anode. This configuration exploits the pH gradient between the acidic catholyte and alkaline anolyte to generate and harvest internal neutralization energy, effectively lowering the electricity demand for electrolysis (Figure 4a). The AHSE employs a Co-Ni₂P/NF anode and Ru-loaded Cu nanowires grown on copper foam (Ru-Cu NW/CF) as the cathode. The Ru-Cu NW/CF cathode achieves a low

overpotential of 207 mV and good durability over 420 h at 500 mA cm⁻² for HER in seawater containing 0.5 M H₂SO₄ (Figure S15, Supporting Information). The anolyte in AHSE consists of 1.0 M KOH containing 0.1 M BA while the catholyte comprises seawater with 0.5 M H₂SO₄, separated by a cation exchange membrane (CEM) to prevent direct acid-base neutralization. By leveraging internal neutralization energy, the AHSE achieves simultaneous production of hydrogen and Ph-COOH at a low cell voltage of 0.98 V at a large current density of 500 mA cm⁻², minimizing electricity expense of 3.16–3.78 kWh per m³ H₂ (Figure 4b). Compared to a hybrid seawater electrolyzer (HSE), which integrates BOR and HER under alkaline conditions, the AHSE reduces the cell voltage by 0.69 V, enabling an energy saving of 24.6–30.6%. This potential reduction is close to the theoretical value of 0.828 V at a pH gradient of 14, showing 83.3% utilization of internal neutralization energy in AHSE. The AHSE can further cut cell voltage by 1.1 V to reduce electricity expense by 39.2–48.7% relative to alkaline water electrolysis (AWE).

During long-term operation, the AHSE exhibits average cell voltages of 1.32–1.58 V (without *iR* correction) at 500 mA cm⁻² and 1.98–2.45 V (without *iR* correction) at twice higher current density of 1,000 mA cm⁻² for 4100 h (Figure 4c). Periodic voltage fluctuations observed during durability tests are attributed to scheduled electrolyte replenishment. The FE of anodic BOR remains ca. 97.7% at 500 mA cm⁻² and ca. 91.3% at 1,000 mA cm⁻² with Ph-COOH selectivity of ca. 95.5% and ca. 78.5% on average, respectively. The decline in Ph-COOH selectivity with increasing current density is attributed to the enhanced formation of Ph-CHO as a by-product, as confirmed by HPLC analysis at various charge inputs at 500–1000 mA cm⁻² (Figure S16, Supporting Information). This increase in Ph-CHO yield arises from the kinetically accelerated electrochemical conversion of Ph-CH₂O* to Ph-CHO* at higher current densities (Figure 3j). The FE for cathodic HER consistently exceeds 97%, enabling hydrogen production at a fast rate of 18.1 mmol h⁻¹ cm⁻² at 1,000 mA cm⁻² (Figure S17, Supporting Information). Post-mortem analysis of SEM, XRD, XPS, elemental mapping, and ICP collectively reveals the deep reconstruction of Co-Ni₂P into amorphous Co-doped Ni(OH)_x after long-term electrolysis, with minor loss of Ni (1.46%) and Co (0.34%) (Figure S18 and Table S5, Supporting Information). The Ph-COOH products can be readily precipitated with 99.3% purity by simply mixing the anolyte and catholyte, requiring a minor acidic supplement (ca. 9.1 vol.% vs HSE) (Figure S19, Supporting Information). Beyond BOR, the AHSE can also effectively convert other water-soluble alcohols (e.g., 1,2-propanediol, ethylene glycol, ethanol) into valuable carboxylic acids with high FE of 91.6–97.6% and 86.4–95% selectivity at 500 mA cm⁻² under 1.4–1.75 V (Figure S20, Supporting Information). When scaled up 100 fold in electrode area (100 cm²), the AHSE can achieve an ultra-high current of 50 A at a low cell voltage of 3.14 V (without *iR* correction). It enables a fast rate of hydrogen production at 0.84 mol h⁻¹ (18.7 L h⁻¹) and BA conversion at 0.4 mol h⁻¹, with over 85% FE for BA conversion and 88.5% Ph-COOH selectivity, demonstrating great industrial feasibility (Figure 4d; Figure S21, Supporting Information). The AHSE demonstrates exceptional durability for large-current electrolysis, surpassing reported hybrid water electrolysis systems that couple anodic oxidation of organics, including benzyl alcohol (BOR), benzylamine (BAOR), 5-hydroxymethylfurfural (HMFOR), methanol (MOR),

ethanol (EOR), potassium lactate (LOR), glycerol (GOR), ethylene glycol (EGOR), and urea (UOR) (Figure 4e; Table S6, Supporting Information).

BA is a key industrial feedstock with annual global production exceeding 305000 tons.^[47] It is widely used in coatings, fragrances, and pharmaceuticals, which often discharge waste steam containing high BA residue over 14 g L⁻¹.^[48] This concentration is roughly equivalent to 0.12 M, aligning well with the substrate requirement of AHSE. Utilizing BA-containing waste as a low-cost feedstock for AHSE thus presents an economically viable approach for cost-effective hydrogen and Ph-COOH production with added environmental benefits. A rough techno-economic analysis (TEA) suggests that the hydrogen cost via AHSE is expected to be reduced to \$0.11 per m³ H₂, achieving 60% of the U.S. Department of Energy (DOE) 2026 target, assuming the use of BA-containing waste (Figure 4f; Table S7, Supporting Information).^[49] It estimates a cost of \$1179.86 ton⁻¹ for Ph-COOH production, which is potentially reduced to \$72.96 ton⁻¹ if assuming waste streams containing BA are used as feedstock. These values compare favorably with conventional liquid-phase oxidation of toluene to Ph-COOH at a higher cost of \$1448.88 ton⁻¹ under high temperature and pressure. Moreover, low toluene conversion (<70%) of the conventional route causes considerable separation costs for unreacted toluene. In contrast, the electro-synthesis approach offers near-quantitative BA conversion with electricity input, significantly enhancing processing efficiency. The upgradation of BA into value-added chemicals potentially offsets 57.8% of the electricity cost, reducing hydrogen production expense by 59.4% compared to AWE. On this basis, capturing the huge neutralization energy of acid and alkaline wastewater through AHSE may unlock further economic and environmental benefits, advancing sustainable hydrogen production and fine chemical synthesis.

3. Conclusion

An asymmetric hybrid system of electrolysis is engineered by integrating acidic HER in seawater with alkaline BOR, effectively harnessing internal neutralization energy for energy-saving hydrogen and benzoic acid production. Utilizing a Co-doped Ni₂P-based electrode, the system achieves an FE of 95.7–98.3% for alkaline BOR with high Ph-COOH selectivity of 95.4–97.4% in a potential range of 1.4–1.8 V. Mechanistic analysis reveals that Co doping plays a vital role in enhancing BOR by promoting the formation of γ-NiOOH as an active intermediate toward BOR, facilitating interfacial charge transfer while shifting the rate-limiting step from the sluggish chemical hydration of Ph-CHO* to efficient electrochemical carbonylation of Ph-CH₂O*. The AHSE significantly reduces electricity consumption to 3.19–3.78 kWh per m³ H₂, enabling simultaneous hydrogen and benzoic acid production at a low cell voltage of 0.98 V at 500 mA cm⁻². The system exhibits exceptional durability for 4,100 h stable electrolysis with 91.3–97.7% FE for BOR at industrial-level current densities of 500–1000 mA cm⁻². Upon scaling up for 100 folds, the AHSE operates at an ultra-high current of 50 A, achieving a hydrogen production rate of 18.7 L h⁻¹ and a benzyl alcohol conversion rate of 0.4 mol h⁻¹ with 88.5% Ph-COOH selectivity. A preliminary techno-economic analysis suggests that integrating

electrocatalytic benzyl alcohol upgrading potentially lowers hydrogen production cost by 59.4% compared to alkaline water electrolysis. Beyond BOR, this versatile system efficiently catalyzes the conversion of various water-soluble alcohols, demonstrating broad applicability and industrial viability.

Supporting Information

Supporting Information is available from the Wiley Online Library or from the author.

Acknowledgements

This work was supported by the National Natural Science Foundation of China (No. 52372175), the Science and Technology Major Project of Liaoning Province (Grant No. 2024JH1/11700013), and the Fundamental Research Funds for the Central Universities (DUT24ZD406, DUT22LAB601). The authors appreciate Dr. Leijie Zhang (Speccreation Instruments Co., Ltd.) for his assistance with XAFS analysis by Table XAFS-500A.

Conflict of Interest

The authors declare no conflict of interest.

Data Availability Statement

The data that support the findings of this study are available in the supplementary material of this article.

Keywords

alcohols electro-refinery, asymmetric hybrid electrolysis, hydrogen production

Received: April 23, 2025

Revised: May 25, 2025

Published online:

- [1] International Energy Agency, Global Hydrogen Review 2023, <https://www.iea.org/reports/global-hydrogen-review-2023> (accessed: March 2023).
- [2] H. Xie, Z. Zhao, T. Liu, Y. Wu, C. Lan, W. Jiang, L. Zhu, Y. Wang, D. Yang, Z. Shao, *Nature* **2022**, 612, 673.
- [3] Y. Liu, Y. Wang, P. Fornasiero, G. Tian, P. Strasser, X. Y. Yang, *Angew. Chem., Int. Ed.* **2024**, 136, 202412087.
- [4] Q. Sha, S. Wang, L. Yan, Y. Feng, Z. Zhang, S. Li, X. Guo, T. Li, H. Li, Z. Zhuang, D. Zhou, B. Liu, X. Sun, *Nature* **2025**, 639, 360.
- [5] H. Jin, J. Xu, H. Liu, H. Shen, H. Yu, M. Jaroniec, Y. Zheng, S. Qiao, *Sci. Adv.* **2023**, 9, ad17755.
- [6] L. Liao, D. Li, Y. Zhang, Y. Zhang, F. Yu, L. Yang, X. Wang, D. Tang, H. Zhou, *Adv. Mater.* **2024**, 36, 2405852.
- [7] J. Guo, Y. Zheng, Z. Hu, C. Zheng, J. Mao, K. Du, M. Jaroniec, S. Qiao, T. Ling, *Nat. Energy* **2023**, 8, 1418.
- [8] M. Ning, F. Zhang, L. Wu, X. Xing, D. Wang, S. Song, Q. Zhou, L. Yu, J. Bao, S. Chen, Z. Ren, *Energy Environ. Sci.* **2022**, 15, 3945.
- [9] H. Shi, T. Wang, J. Liu, W. Chen, S. Li, J. Liang, S. Liu, X. Liu, Z. Cai, C. Wang, D. Su, Y. Huang, L. Elbaz, Q. Li, *Nat. Commun.* **2023**, 14, 3934.
- [10] C. Tang, Y. Zheng, M. Jaroniec, S. Z. Qiao, *Angew. Chem., Int. Ed.* **2021**, 60, 19572.
- [11] Y. Li, X. Wei, L. Chen, J. Shi, *Angew. Chem., Int. Ed.* **2021**, 60, 19550.
- [12] F. Meng, Q. Wu, K. Elouarzaki, S. Luo, Y. Sun, C. Dai, S. Xi, Y. Chen, X. Lin, M. Fang, X. Wang, D. Mandler, Z. J. Xu, *Sci. Adv.* **2023**, 9, adh9487.
- [13] X. Fu, J. B. Pedersen, Y. Zhou, M. Saccoccio, S. Li, R. Sažinas, K. Li, S. Z. Andersen, A. Xu, N. H. Deissler, J. B. V. Mygind, C. Wei, J. Kibsgaard, P. C. K. Vesborg, J. K. Nørskov, I. Chorkendorff, *Science* **2023**, 379, 707.
- [14] P. Wang, A. Pei, Z. Chen, P. Sun, C. Hu, X. Wang, N. Zheng, G. Chen, *Nat. Commun.* **2025**, 16, 731.
- [15] Z. Yu, L. Liu, *Adv. Mater.* **2024**, 36, 2308647.
- [16] T. Wang, Z. Huang, T. Liu, L. Tao, J. Tian, K. Gu, X. Wei, P. Zhou, L. Gan, S. Du, Y. Zou, R. Chen, Y. Li, X. Z. Fu, S. Wang, *Angew. Chem., Int. Ed.* **2022**, 61, 202115636.
- [17] Y. Yan, H. Zhou, S. M. Xu, J. Yang, P. Hao, X. Cai, Y. Ren, M. Xu, X. Kong, M. Shao, Z. Li, H. Duan, *J. Am. Chem. Soc.* **2023**, 145, 6144.
- [18] W. R. Leow, Y. Lum, A. Ozden, Y. Wang, D. H. Nam, B. Chen, J. Wicks, T. T. Zhuang, F. Li, D. Sinton, E. H. Sargent, *Science* **2020**, 368, 1228.
- [19] W. Li, H. Jiang, X. Zhang, B. Lei, L. Li, H. Zhou, M. Zhong, *J. Am. Chem. Soc.* **2024**, 146, 21968.
- [20] Y. Meng, E. Gnanamani, R. N. Zare, *J. Am. Chem. Soc.* **2023**, 145, 17577.
- [21] F. Liu, X. Gao, R. Shi, J. Xiong, Z. Guo, E. C. M. Tse, Y. Chen, *Adv. Funct. Mater.* **2023**, 34, 2310274.
- [22] Q. Qian, Y. Zhu, N. Ahmad, Y. Feng, H. Zhang, M. Cheng, H. Liu, C. Xiao, G. Zhang, Y. Xie, *Adv. Mater.* **2023**, 36, 202306108.
- [23] R. Liu, W. Tu, A. Pei, W. H. Huang, Y. Jia, P. Wang, D. Liu, Q. Wu, Q. Qin, W. Zhou, L. Zhou, K. Yan, Y. Zhao, G. Chen, *J. Am. Chem. Soc.* **2025**, 147, 10339.
- [24] Y. Li, X. Wei, S. Han, L. Chen, J. Shi, *Angew. Chem., Int. Ed.* **2021**, 60, 21464.
- [25] Y. Wu, Z. Yu, Y. Tong, C. Lin, N. Zhang, P. Chen, *Adv. Funct. Mater.* **2025**, <https://doi.org/10.1002/adfm.202502104>.
- [26] G. Zhou, N. Zhang, Z. Huang, J. He, J. Zhu, X. Ren, Y. Tong, H. Wang, P. Chen, *Chem. Eng. J.* **2025**, 503, 158619.
- [27] Z. Li, Y. Yan, S. M. Xu, H. Zhou, M. Xu, L. Ma, M. Shao, X. Kong, B. Wang, L. Zheng, H. Duan, *Nat. Commun.* **2022**, 13, 147.
- [28] S. Li, R. Ma, J. Hu, Z. Li, L. Liu, X. Wang, Y. Lu, G. E. Sterbinsky, S. Liu, L. Zheng, J. Liu, D. Liu, J. Wang, *Nat. Commun.* **2022**, 13, 2916.
- [29] L. Fan, Y. Ji, G. Wang, J. Chen, K. Chen, X. Liu, Z. Wen, *J. Am. Chem. Soc.* **2022**, 144, 7224.
- [30] Q. Qian, X. He, Z. Li, Y. Chen, Y. Feng, M. Cheng, H. Zhang, W. Wang, C. Xiao, G. Zhang, Y. Xie, *Adv. Mater.* **2023**, 35, 2300935.
- [31] Y. Ding, P. Cai, Z. Wen, *Chem. Soc. Rev.* **2021**, 50, 1495.
- [32] F. Sun, D. He, K. Yang, J. Qiu, Z. Wang, *Angew. Chem., Int. Ed.* **2022**, 61, 202203929.
- [33] Z. M. Bhat, D. Pandit, S. Ardo, R. Thimmappa, A. R. Kottaichamy, N. Christudas Dargily, M. C. Devendrachari, M. O. Thotiyl, *Joule* **2020**, 4, 1730.
- [34] C. Zhang, S. Ci, X. Peng, J. Huang, P. Cai, Y. Ding, Z. Wen, *J. Energy Chem.* **2021**, 54, 30.
- [35] J. Li, C. Zhang, C. Zhang, H. Ma, Z. Guo, C. Zhong, M. Xu, X. Wang, Y. Wang, H. Ma, J. Qiu, *Adv. Mater.* **2022**, 34, 2203900.
- [36] P. Wang, J. Zheng, X. Xu, Y. Q. Zhang, Q. F. Shi, Y. Wan, S. Ramakrishna, J. Zhang, L. Zhu, T. Yokoshima, Y. Yamauchi, Y. Z. Long, *Adv. Mater.* **2024**, 36, 2404806.
- [37] W. Chen, C. Xie, Y. Wang, Y. Zou, C. L. Dong, Y. C. Huang, Z. Xiao, Z. Wei, S. Du, C. Chen, B. Zhou, J. Ma, S. Wang, *Chem* **2020**, 6, 2974.
- [38] B. S. Yeo, A. T. Bell, *J. Phys. Chem. C* **2012**, 116, 8394.
- [39] H. L. Huang, C. Yu, X. T. Han, H. W. Huang, Q. B. Wei, W. Guo, Z. Wang, J. S. Qiu, *Energy Environ. Sci.* **2020**, 13, 4990.
- [40] M. M. Billah, Q. Chen, *SN Appl. Sci.* **2019**, 1, 521.

- [41] E. D. Schmid, M. Moschallski, W. L. Peticolas, *J. Phys. Chem.* **1986**, 90, 2340.
- [42] D. S. Hall, D. J. Lockwood, S. Poirier, C. Bock, B. R. MacDougall, *J. Phys. Chem. A* **2012**, 116, 6771.
- [43] R. X. Ge, Y. Wang, Z. Z. Li, M. Xu, S. M. Xu, H. Zhou, K. Y. Ji, F. G. Chen, J. H. Zhou, H. H. Duan, *Angew. Chem., Int. Ed.* **2022**, 61, 202200211.
- [44] P. Zhou, X. Lv, S. Tao, J. Wu, H. Wang, X. Wei, T. Wang, B. Zhou, Y. Lu, T. Frauenheim, X. Fu, S. Wang, Y. Zou, *Adv. Mater.* **2022**, 34, 2204089.
- [45] Y. Yan, R. Wang, Q. Zheng, J. Zhong, W. Hao, S. Yan, Z. Zou, *Nat. Commun.* **2023**, 14, 7987.
- [46] G. Fu, X. Kang, Y. Zhang, Y. Guo, Z. Li, J. Liu, L. Wang, J. Zhang, X. Z. Fu, J. L. Luo, *Nat. Commun.* **2023**, 14, 8395.
- [47] Mordor Intelligence, Benzyl Alcohol Market Size & Share Analysis - Growth Trends & Forecasts (2025 – 2030), <https://www.mordorintelligence.com/industry-reports/benzyl-alcohol-market> (accessed: March 2023).
- [48] Y. Chen, B. Pan, Q. Zhang, *J. Ind. Eng. Chem.* **2007**, 58, 1220.
- [49] US. Department of Energy, *U. S. National Clean Hydrogen Strategy, and Roadmap*, US. Department of Energy, Washington, DC, USA **2023**.